Dalton Transactions

ROYAL SOCIETY OF CHEMISTRY

PAPER

View Article Online
View Journal

Cite this: DOI: 10.1039/d6dt00909c

Geometric control of Fe(I) intermediates in CO_2 photoreduction by tetrahedral tripodal phosphine complexes

Marcos A. Bento,[a] Nuno A. G. Bandeira,[b] Haralampos N. Miras,[c] Sara Realista,[a] Michael Gleeson,[d] Edwin J. Devid,[e] Paula Brandão,[f] João Rocha[f] and Paulo N. Martinho *[a,g]

The development of homogeneous CO_2 photoreduction catalysts based on Earth-abundant metals remains limited due to an insufficient mechanistic understanding of multielectron activation pathways. Here we show that a pseudotetrahedral Fe(II) complex supported by a tripodal tetradentate phosphine ligand, ^{5}[Fe^{II}(**NP^{iso}**)(Cl)](BPh$_4$), functions as an efficient and selective molecular catalyst for visible-light-driven CO_2-to-CO conversion. Under the optimized conditions in acetonitrile, ^{5}[Fe^{II}(**NP^{iso}**)(Cl)](BPh$_4$) achieves turnover numbers exceeding 1300, turnover frequencies of up to 445 h^{-1}, and quantum yields of up to 0.64%, placing it among the most active Fe-based molecular catalysts for CO_2 photoreduction. Electrochemical, spectroelectrochemical, fluorescence quenching, and high-resolution ESI-MS measurements, supported by computational studies, reveal that catalysis proceeds *via* a one-electron-reduced Fe(I) acetonitrile adduct formed by ligand substitution of the Fe(II) precursor. This Fe(I) species promotes CO_2 binding and proton-coupled reduction through well-defined Fe(I/II) intermediates, culminating in CO release and regeneration of the active complex. The CO-release step is found to be the rate-determining step ($\Delta G^{\ddagger}$ = 12.9 kcal mol^{-1}) with the generation of a Fe(II) complex displaying a coordination vacancy. The addition of a new acetonitrile molecule in tandem with one electron reduction regenerates the catalytically active species. These results demonstrate that pseudotetrahedral P_3N coordination environments stabilize reactive Fe(I) intermediates essential for CO_2 activation, offering mechanistic design principles towards next-generation iron catalysts.

Received 20th April 2026,
Accepted 26th May 2026

DOI: 10.1039/d6dt00909c

rsc.li/dalton

Introduction

The photochemical reduction of CO_2 to CO using homogeneous molecular catalysts remains a central challenge in solar-to-fuel chemistry, hence catalysts are required that operate efficiently, selectively, and at low overpotential.[1–4] Although multicomponent approaches featured in the literature coupling a photosensitizer, sacrificial electron donor, and proton source have achieved significant progress, the control of the selectivity and turnover efficiency of these processes, particularly for catalysts based on Earth-abundant metals, remains elusive.[5–13]

Molecular catalysts based on iron, manganese, and cobalt complexes have delivered notable activity in CO_2 photoreduction, with Fe polypyridyl and quaterpyridine complexes in particular achieving turnover numbers (TON) of up to ~3800 and CO selectivity >90% under the optimized conditions.[14–16] Despite these advances, the mechanistic understanding of iron systems lags behind that of their cobalt and manganese counterparts. In particular, the electronic structures and coordination environment of key Fe(I) intermediates, widely proposed to mediate CO_2 binding and C–O bond activation, remain poorly reported.[8,9,17–41]

Work by Peters, Beller, and others has shown that pseudotetrahedral Fe(II) complexes supported by phosphine-rich tripodal ligands exhibit rich redox chemistry, with readily accessible Fe(I) oxidation states, and stabilize both π-acidic and π-basic substrates including CO_2 and N_2.[42–51]

[a]*Centro de Química Estrutural, Institute of Molecular Sciences, Departamento de Química e Bioquímica, Faculdade de Ciências, Universidade de Lisboa, Campo Grande, 1749-016 Lisboa, Portugal. E-mail: pnmartinho@ciencias.ulisboa.pt*
[b]*Biosystems and Integrative Sciences Institute (BioISI), Departamento de Química e Bioquímica, Faculdade de Ciências Universidade de Lisboa, 8.5.53-C8 Campo Grande, 1749-016 Lisboa, Portugal*
[c]*School of Chemistry, The University of Glasgow, Glasgow G12 8QQ, UK*
[d]*Dutch Institute for Fundamental Energy Research (DIFFER), De Zaale 20, 5612 AJ Eindhoven, The Netherlands*
[e]*KapiteinLabs, Koepelplein 1E, 2031 WL Haarlem, The Netherlands*
[f]*Department of Chemistry, CICECO-Aveiro Institute of Materials, University of Aveiro, 3810-193 Aveiro, Portugal*
[g]*Max Planck Institute for the Science of Light, Staudtstr. 2, 91058 Erlangen, Germany*

Previous investigations of tripodal phosphine-supported iron complexes (FeP_3) have established the structural and mechanistic principles that show their subsequent development in carbon dioxide reduction chemistry. Rigid FeP_3 complexes stabilise low-coordinate Fe(II) centres preserving labile sites for substrate binding or insertion. These systems show that carbon dioxide insertion into Fe–H bonds generates formate-derived intermediates and they were investigated principally for stoichiometric small-molecule activation and mechanistic insight rather than catalytic CO_2 reduction. In related tripodal phosphine-supported first-row transition-metal complexes, catalytic CO_2 hydrogenation has been achieved with turnover numbers in the range of 7500, depending on the proton source, reducing agent, and ligand design.[47–53]

These properties suggest that such complexes may favor multielectron activation steps relevant to CO_2 reduction; however, their photochemical behavior and mechanistic pathways under CO_2 photoreduction conditions have not been established.[42,44,52–56]

Motivated by these previous studies, we investigated the photochemical CO_2 reduction chemistry of a pseudotetrahedral Fe(II) complex supported by the tetradentate tripodal phosphine ligand **NP^{iso}**, ^{5}[Fe^{II}(**NP^{iso}**)(Cl)](BPh$_4$) (herein the superscripted prefix denotes the spin multiplicity) previously synthesised and characterised by MacBeth and co-workers (Fig. 1).[48] The fluxionality of the **NP^{iso}** ligand scaffold is such that it allows unstable tetrahedral structures to revert easily to a trigonal bipyramidal coordination environment and possible spin state change along the catalytic route. We hypothesized that the P_3N coordination environment would stabilize reduced Fe(I) intermediates competent for CO_2 binding and proton-coupled electron transfer.

Here, we report that ^{5}[Fe^{II}(**NP^{iso}**)(Cl)](BPh$_4$) is an efficient and selective catalyst for the visible-light-driven CO_2-to-CO conversion, achieving TON values in excess of 1300 at micromolar catalyst concentrations. Through a combination of electrochemical, spectroscopic, and computational analyses, we identify key Fe(I/II) intermediates and propose a mechanistic cycle involving CO_2 protonation and Fe(I)-mediated C–O bond cleavage. These findings demonstrate that four-coordinate, distorted ("pseudotetrahedral") P_3N-supported Fe complexes afford catalytically relevant Fe(I) species *via* photocatalytic electron relay through a sacrificial electron donor and enable direct observation of reduction, CO_2-binding, and CO-release steps, making them attractive scaffolds for rational catalyst design.

Results and discussion

Synthesis and characterization of ^{5}[Fe^{II}(NP^{iso})(Cl)](BPh$_4$)

Crystals of ^{5}[Fe^{II}(**NP^{iso}**)(Cl)](BPh$_4$) were isolated in high purity and characterized by X-ray crystallography, elemental analysis, NMR and FTIR spectroscopy (Fig. S1 to S6). The data confirm the presence of a high-spin Fe(II) center in a distorted pseudotetrahedral geometry as described by Peters and co-workers.[48] ^{5}[Fe^{II}(**NP^{iso}**)(Cl)](BPh$_4$) crystallized in the triclinic space group $P\bar{1}$ and displays an elongated Fe–N distance of 2.695 Å and Fe–P distances of 2.466, 2.491 and 2.486 Å. The Fe(II) center lies slightly above the P_3 ligand plane and displays P–Fe–Cl angles of 105.28°, 104.30° and 115.68° (τ_4 = 0.92), consistent with the expected pseudotetrahedral distortion. Comparison of the powder X-ray diffraction pattern of the synthesized material with the simulated pattern derived from single-crystal data confirms that the crystals obtained are representative of the bulk sample (Fig. S7 and S8, Table S1).

The UV-vis spectrum of ^{5}[Fe^{II}(**NP^{iso}**)(Cl)](BPh$_4$) in acetonitrile (MeCN) exhibits three π–π* intraligand bands at 195, 266 and 297 nm (Fig. S9). Cyclic voltammetry (CV) under a N_2 atmosphere reveals solvent-dependent redox behavior. In 1,2-dichloroethane (DCE) an irreversible oxidation is observed at 0.36 V *vs.* Fc/Fc$^+$ and a reversible Fe$^{II/I}$ redox process at $E_{1/2}$ = −1.64 V *vs.* Fc/Fc$^+$ (Fig. S10), consistent with the results previously reported in tetrahydrofuran (THF) by Peters and co-workers.[48] In MeCN, an irreversible oxidation occurs at 0.53 V *vs.* Fc/Fc$^+$ with a reversible Fe$^{II/I}$ redox process at $E_{1/2}$ = −1.53 V *vs.* Fc/Fc$^+$ as observed when using THF and DCE as solvents. A new reversible Fe$^{II/I}$ redox process was observed at $E_{1/2}$ = −2.17 V *vs.* Fc/Fc$^+$ which was attributed to the formation of the complex ^{4}[Fe^{I}(**NP^{iso}**)(MeCN)]$^+$, consistent with the DFT calculations described below. Scan-rate analysis supports an ECE mechanism for the first reduction wave in both solvents, evidenced by $ip/\nu^{1/2}$ deviation from diffusion-controlled behavior

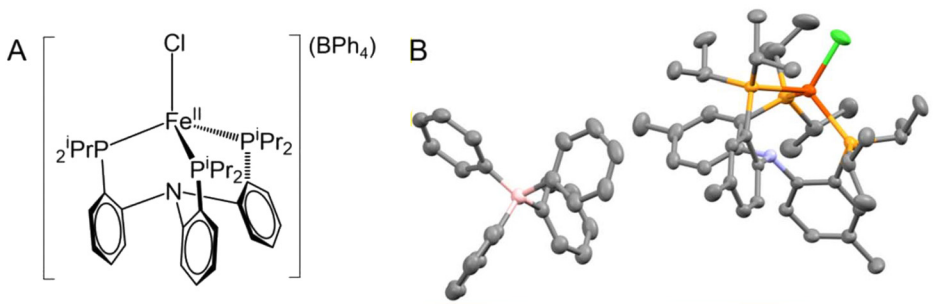

Fig. 1 Schematic representation of ^{5}[Fe^{II}(**NP^{iso}**)(Cl)](BPh$_4$) (panel A) and the X-ray crystal structure of ^{5}[Fe^{II}(**NP^{iso}**)(Cl)](BPh$_4$) (panel B). Legend: Fe (dark orange); Cl (green); P (light orange); N (blue); C (grey); B (pink). Hydrogens were omitted for clarity.

and consistent with ligand dissociation or MeCN coordination (Fig. S12–S14).[57]

The CV studies under a CO_2 atmosphere in a solution of $^5[Fe^{II}(\mathbf{NP^{iso}})(Cl)](BPh_4)$ in DCE did not show any change from the results obtained under a N_2 atmosphere, demonstrating that no catalytic current enhancement is observed, indicating that CO_2 reduction is not triggered in DCE (Fig. S15 and S16). In contrast, $^5[Fe^{II}(\mathbf{NP^{iso}})(Cl)](BPh_4)$ in MeCN shows a current increase around −2.17 V *vs.* Fc/Fc^+ which increases further with the addition of H_2O used as a proton source, indicating that $^5[Fe^{II}(\mathbf{NP^{iso}})(Cl)](BPh_4)$ can be a promising catalyst for CO_2 reduction reaction under these conditions (Fig. 2).[31] These results motivated subsequent evaluation of $^5[Fe^{II}(\mathbf{NP^{iso}})(Cl)](BPh_4)$ for photochemical CO_2 reduction in MeCN (*vide infra*).

Catalytic performance of $^5[Fe^{II}(\mathbf{NP^{iso}})(Cl)](BPh_4)$ in the CO_2 photoreduction reaction

$^5[Fe^{II}(\mathbf{NP^{iso}})(Cl)](BPh_4)$ was evaluated as a catalyst for the CO_2 photoreduction reaction under blue LED irradiation ($\lambda \approx$ 480 nm) at room temperature. A CO_2-saturated MeCN solution containing the PS $[Ir(dtbbpy)(ppy)_2](PF_6)$ (0.2 mM), the sacrificial electron donor (SED), 1,3-dimethyl-2-phenyl-2,3-dihydro-1*H*-benzo[*d*]imidazole (BIH) (0.1 M), phenol (1 M, proton source), and $^5[Fe^{II}(\mathbf{NP^{iso}})(Cl)](BPh_4)$ (0.5 μM) produced 2.96 μmol CO after 3 h, corresponding to TON_{CO} = 1183 (TOF_{CO} = 394 h^{-1}), with a selectivity of 37% for CO over H_2 production and a quantum yield for the CO formation (Φ_{CO}) of 0.57%. The detailed optimization of the photoreduction conditions is displayed in Tables S2 and S3. Table S2 summarizes control experiments performed with catalyst concentrations ranging from 0.5 to 50 μM, showing that the TON, turnover frequency (TOF) and CO_2-to-CO selectivity all increase as the catalyst concentration decreases (Fig. 3 and Table S2, entries 1–3). Photoreduction experiments conducted over time intervals from 1 to 360 min show that CO production reaches its maximum after 3 h (Fig. 3 and Fig. S17). The photoreduction activity increases markedly upon addition of H_2O as a mild proton donor, producing 3.34 μmol CO after 3 h, corresponding to TON_{CO} = 1335 and TOF_{CO} = 445 h^{-1}, with 86% CO_2-to-CO selectivity and Φ_{CO} = 0.64%. In contrast, the use of stronger Brønsted acids such as phenol leads to diminished CO selectivity and enhanced H_2 formation, consistent with previous reports of related tripodal Fe(II) frameworks, where strong acids promote preferential H_2 evolution.[3,6–14] An alcoholic proton donor, iPrOH, afforded only trace amounts of CO under identical irradiation conditions, further supporting that for this system CO production is favored by protic, coordinating, and weakly acidic media in MeCN. Taken together, these results show that the P_3N ligand scaffold stabilizing the Fe(II) center improves the catalytic activity and selectivity for CO_2 reduction to CO in MeCN, particularly when combined with a mild and soluble proton donor.

The use of an electron mediator (EMD) in CO_2 photoreduction systems was previously reported using organic molecules,

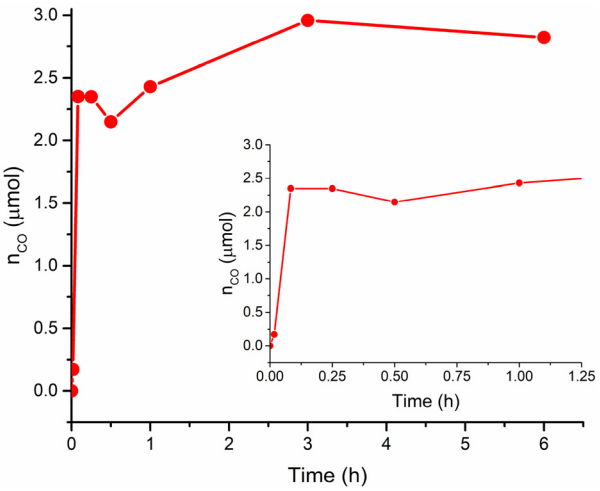

Fig. 3 Irradiation-time dependence of CO formation catalyzed by $^5[Fe^{II}(\mathbf{NP^{iso}})(Cl)](BPh_4)$. Reactions were performed in a CO_2-saturated MeCN solution containing $^5[Fe^{II}(\mathbf{NP^{iso}})(Cl)](BPh_4)$, $[Ir(dtbbpy)(ppy)_2](PF_6)$ (0.2 mM), BIH (0.1 M) and phenol (1 M), under blue LED irradiation (30 W) for up to 3 h.

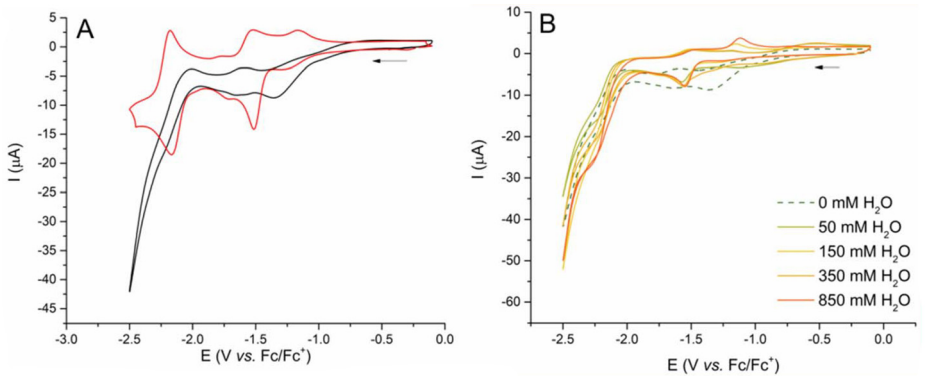

Fig. 2 Cyclic voltammogram overlay of $^5[Fe^{II}(\mathbf{NP^{iso}})(Cl)](BPh_4)$: under a N_2 atmosphere (red) and under a CO_2 atmosphere (black) in MeCN (panel A) and under a CO_2 atmosphere in MeCN with different H_2O concentrations (panel B). $TBAPF_6$ was used as the supporting electrolyte (0.1 M). Glassy carbon (3 mm diameter) was used as the working electode, platinum wire as the counter electrode and Ag/Ag^+ as the reference electrode. Fc was used as the internal standard.

such as tri-*p*-tolylamine (TTA) or molecular complexes, for example ferrocene (Fc).[58–60] The studies performed by Shan and Schmehl and Fujita demonstrated efficient reductive quenching of the excited state of $[Ru(bpy)_3]^{2+}$ using TTA as an EMD and triethylamine as the sacrificial electron donor in MeCN.[58,59] Inspired by this mediator paradigm, CO_2 photoreduction was subsequently examined for $^5[Fe^{II}(\mathbf{NP^{iso}})(Cl)](BPh_4)$ in coordinating, protic MeCN using the PS complex $[Ir(dtbbpy)(ppy)_2](PF_6)$ (0.2 mM), BIH (SED, 0.1 M) and phenol (1 M, proton source). Incorporation of TTA (7.27 mM) showed an increase in the CO production compared with the results described earlier (Table S2), achieving 3.80 μmol CO after 3 h (TON_{CO} = 1520, TOF_{CO} = 507 h^{-1} and Φ_{CO} = 0.73%) (Table 1, entries 1–4). Control experiments excluding BIH yielded only trace amounts of CO (Table 1, entries 5 and 6), supporting a mediator role for TTA rather than direct SED function under these conditions. These results highlight the electronic transfer ability of TTA improving the catalytic efficiency of the system. With Fc as an EMD, $^5[Fe^{II}(\mathbf{NP^{iso}})(Cl)](BPh_4)$ produced 3.22 μmol CO after 3 h, improving the amount of CO in comparison with the results obtained without EMD in the system (Table 1, entries 7 and 8). In contrast, MeCN : H_2O (4.5 : 0.5) with Fc suppressed CO formation and lowered Φ_{CO}, consistent with dominant deactivation pathways potentially linked to H_2O-derived ROS for Fc-mediated systems.[60–64] Limited solubility of TTA in MeCN : H_2O led to precipitation at concentrations higher 10 mM, precluding reliable mediated photoreduction analysis in this solvent mixture.

These results highlight the importance of electron mediators in photoreduction systems, demonstrating that catalytic activity is enhanced in their presence. Compared with Fe tetra-porphyrin benchmarks reported by Bonin and co-workers (Φ_{CO} = 1 × 10^{-3}%), our system delivers substantially higher activity, achieving quantum yields of up to Φ_{CO} = 0.73% within a similar concentration range.[34] In a broader context, Fe porphyrins and related Fe macrocycles represent one of the benchmark catalyst families for molecular CO_2 reduction typically achieving high selectivity toward CO formation. For example, Fe(II)-polypyridyl complexes are some of the catalysts studied for the CO_2 electrochemical reduction reaction achieving faradaic efficiencies of up to 97% and turnover numbers of up to 3.6 × 10^8 after 1 h, across a range of applied potentials (between −1.35 to −1.98 V *vs.* Fc/Fc^+). However, these benchmark Fe systems are predominantly used for electrochemical CO_2 reduction rather than purely photochemical CO_2 reduction, and therefore direct comparison with quantum yield metrics is not straightforward.

In photochemical CO_2 reduction Fe-based systems generally exhibit significantly lower efficiencies since the overall activity depends not only on catalytic turnover, but also on light absorption and excited-state quenching. Nevertheless, several Fe photoreduction systems have been studied in recent years. For example, Guo and co-workers reported an Fe(II) quaterpyridine catalyst combined with $[Ru(bpy)_3]Cl_2$ as a photosensitizer and BIH as a sacrificial donor in MeCN/TEOA, achieving Φ_{CO} values of up to 8.8%, TONs of 1879, and CO selectivities of 92%. In the same study, replacement of the Ru photosensitizer with the organic dye purpurin still enabled selective CO_2-to-CO conversion, with TONs of 1365 and Φ_{CO} = 1.1%, representing one of the most efficient Fe-based CO_2 photoreduction systems reported to date.[26] Within this broader context, the results obtained in the present work demonstrate that the turnover numbers and quantum efficiencies using $^5[Fe^{II}(\mathbf{NP^{iso}})(Cl)](BPh_4)$ are comparable to many previously reported Fe photoreduction systems, significantly outperforming classical Fe tetraporphyrin benchmarks while reaching the efficiency range of the best-performing Fe molecular catalysts for CO_2 photoreduction reported in the literature (Table 2).[6,26,31,34]

Table 1 Optimization of the electron mediator component in the catalytic CO_2 reduction reaction

Entry	n_{H_2} [μmol]	$\langle b \rangle n_{CO}$ [μmol]	$Selectivity_{CO}$ [%]	TON_{CO}	TOF_{CO} [h^{-1}]	Φ_{CO} [%]
1[a]	3.47	1.35	—	—	—	—
2	5.11	2.96	37	1183	394	0.57
3[a,b]	3.74	1.38	—	—	—	—
4[b]	10.09	3.80	27	1520	507	0.73
5[a,c]	tr.	tr.	—	—	—	—
6[c]	tr.	tr.	—	—	—	—
7[a,d]	6.15	1.38	—	—	—	—
8[d]	11.51	3.22	22	1285	428	0.62
9[a,e]	0.74	0.66	—	—	—	—
10[e]	0.08	2.20	96	881	294	0.42

In a typical run, a CO_2-saturated MeCN solution containing $^5[Fe^{II}(\mathbf{NP^{iso}})(Cl)](BPh_4)$ (0.5 μM), $[Ir(dtbbpy)(ppy)_2](PF_6)$ (0.2 mM), BIH (0.1 M) and phenol (1 M) was irradiated using blue LED strip light (30 W) for 3 h under a CO_2 atmosphere. [a] Without a catalyst. [b] Using TTA (7.27 mM) as the EMD. [c] Using TTA (7.27 mM) as the EMD and without BIH. [d] Using Fc (7.27 mM) as the EMD. [e] Using Fc (7.27 mM) as the EMD in 4.5 : 0.5 (MeCN : H_2O). For the quantum yield calculation to the CO formation, the number of photons was calculated using the $K_3[Fe(C_2O_4)_3]$ actinometer method (2.63 × 10^{17} photons per second).[32]

Mechanistic studies

The solvent-dependent CO_2 photoreduction activity of $^5[Fe^{II}(\mathbf{NP^{iso}})(Cl)](BPh_4)$ prompted a detailed mechanistic investigation using spectroscopy, spectroelectrochemistry, mass spectrometry, and DFT calculations.

To probe the quenching mechanism, we performed Stern–Volmer analysis of the excited state of $[Ir(dtbbpy)(ppy)_2](PF_6)$ ($E(^*Ir^{III}/Ir^{II})$ = +0.6 V *vs.* Fc/Fc^+) using BIH ($E(BIH/BIH^+)$ = −0.07 V *vs.* Fc/Fc^+) and $^5[Fe^{II}(\mathbf{NP^{iso}})(Cl)](BPh_4)$ ($E(Fe^{II}/Fe^{III})$ = 0.53 V and $E(Fe^{II}/Fe^{I})$ = −1.53 V *vs.* Fc/Fc^+) as potential quenchers. The bimolecular quenching rate constants (k_q) obtained for BIH and $^5[Fe^{II}(\mathbf{NP^{iso}})(Cl)](BPh_4)$ are 9.93 × 10^8 M^{-1} s^{-1} and 0 M^{-1} s^{-1}, respectively, indicating that the system operates *via* a reductive quenching pathway mediated by BIH (Fig. S18 to S21). Electron transfer quenching of $[Ir(dtbbpy)(ppy)_2](PF_6)$ by TTA ($E(TTA/TTA^+)$ = +0.45 V *vs.* Fc/Fc^+) was also examined, the data followed Stern–Volmer kinetics. The k_q obtained for TTA is 1.16 × 10^9 M^{-1} s^{-1} and indicates that the system follows a reductive quenching pathway (Fig. S22 and S23).[65,66]

Table 2 Comparison between the Fe(II) complex studied in this work and other Fe CO_2 photoreduction systems

Entry	Catalyst	PS	SED	TON_{CO}	Φ_{CO} [%]	$Selectivity_{CO}$ [%]	Ref.
1	$^5[Fe^{II}(NP^{iso})(Cl)]^{2+}$	$[Ir(dtbbpy)(ppy)_2]^+$	BIH	1335	0.64	86	This work
2	$[Fe^{II}(dmp)_2(NCS)_2]$	$[Cu^I(dmp)(P)_2]^+$	TEOA-BIH	273	6.7	78	6
3	$[Fe(qpy)(H_2O)_2]^{2+}$	$[Ru(bpy)_3]^{2+}$	BIH	3844	—	85	26
4	$[Fe(tpyPY2Me)]^{2+}$	$[Ru(bpy)_3]^{2+}$	BIH	15 520	11.1	99	31
5	[Fe(TPP)]	$[Ir(ppy)_3]$	TEA	140	1×10^{-3}	93	34

Ligand abbreviations list according to the literature: dmp = 2,9-dimethyl-1,10-phenanthroline; P = phosphine ligand with tethered 2,9-positions of phenanthroline (phen) and bathophenanthroline (baphen) with propyl chains; qpy = 2,2′:6′,2″:6″,2‴-quaterpyridine; bpy = bipyridine; tpyPY2Me = 6-(1,1-di(pyridin-2-yl)ethyl)-2,2′:6′,2″-terpyridine; TPP = 5,10,15,20-tetrakis(2′,6′-dihydroxyphenyl)porphyrin; ppy = 2-phenylpyridine.

Considering that TTA has a higher k_q in relation to BIH, it is anticipated that TTA might act as a SED. However, back electron transfer from TTA to $[Ir(dtbbpy)(ppy)_2](PF_6)$ was previously observed for similar systems, matching the results presented in the CO_2 photoreduction section.[59]

Infrared spectroelectrochemistry (SEC-IR) under a N_2 atmosphere provides evidence for solvent-enabled intermediate formation. At the primary Fe(II/I) reduction of $^5[Fe^{II}(\mathbf{NP^{iso}})(Cl)](BPh_4)$ (−1.65 V *vs.* Ag pseudoreference, DCE/MeCN), the ligand C=C band at 1610 cm^{-1} disappears, and no new, well-defined metal-bound vibrations emerge, indicating that the initial complex is consumed to form other species in solution (Fig. S24). The formation of $^4[Fe^{I}(\mathbf{NP^{iso}})(NCMe)]^+$ is observed in a 5 mM solution of $^5[Fe^{II}(\mathbf{NP^{iso}})(Cl)](BPh_4)$ in DCE/MeCN under an N_2 atmosphere at the second reduction (−2.30 V *vs.* Ag pseudoreference), which is characterized by a C=C vibration at 1723 cm^{-1} and a Fe–CN vibration at 2337 cm^{-1} (Fig. 4A). This frequency is similar to that found for the Fe–CN vibration in Fe(PNP) compounds.[57,61–64] Decrease of the free-MeCN C≡N band (2307 cm^{-1}) further supports MeCN coordination and formation of the MeCN-adduct $^4[Fe^{I}(\mathbf{NP^{iso}})(NCMe)]^+$.

Under a CO_2 atmosphere in MeCN, the Fe–CO vibrations at 1884 cm^{-1} (−1.85 V *vs.* Ag, MeCN, 5 mM) indicate the formation of the one-electron-reduced carbonyl adduct $[Fe^{I}(\mathbf{NP^{iso}})(CO)]^+$ reported for related Fe(I) complexes (Fig. 4B and Fig. S25).[48] Comparative SEC-IR under N_2 at the second reduction (−1.85 V *vs.* Ag pseudoreference) shows only baseline ligand absorptions, indicating that carbonylation is CO_2-dependent, supporting its assignment to electrochemical CO_2 reduction rather than solvent-only processes (Fig. S26).[67–71]

High-resolution ESI-MS was used to profile the composition of the catalytic mixture in solution, targeting persistent species relevant to the CO_2 photoreduction cycle in the 600–1000 *m*/*z* range.[72–75] These species can be linked to two potential reaction pathways: the protonation and disproportionation of CO_2, consistent with the experimental data discussed above, and the proposed mechanistic cycle shown in Fig. 5 and 6 below. The ESI-MS studies were performed in MeCN : H_2O solution in positive ionization mode. During the CO_2 photoreduction experiments, a 5 mL MeCN/H_2O (4.5 mL of MeCN to 0.5 mL of H_2O) solution of $^5[Fe^{II}(\mathbf{NP^{iso}})(Cl)](BPh_4)$ (50 μM), containing $[Ir(dtbbpy)(ppy)_2](PF_6)$ (0.2 mM) and 0.1 M BIH were used as PS and SED, respectively. Subsequently, the solution was irradiated in a quartz cell using a low voltage halogen lamp (100 W) for 3 hours.

Interestingly, the isotopic distribution envelopes at *m*/*z* 690.40 and 773.30 correspond to the cations of the intact complex $\{Fe^{I}(P^{iso})\}^+$ and to the MeCN adduct $\{[Fe^{I}(P^{iso})$

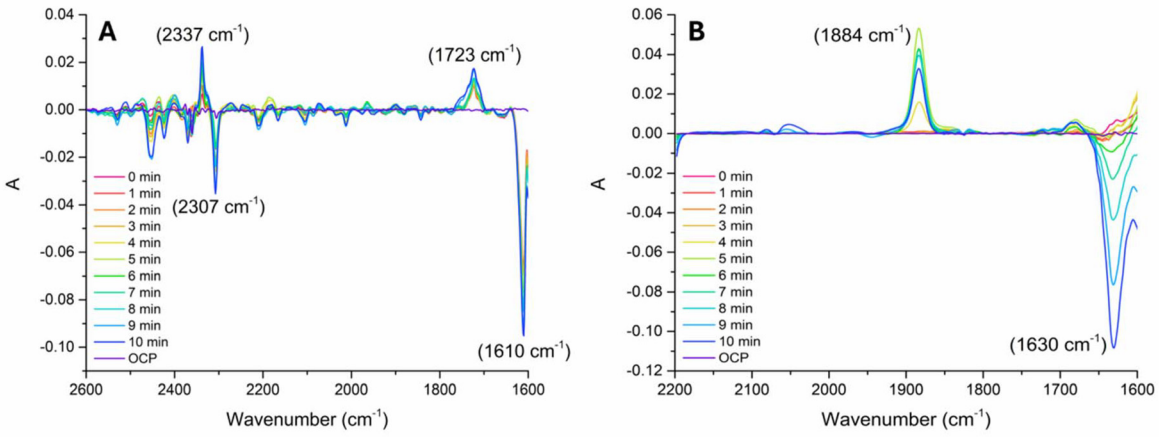

Fig. 4 SEC-IR experiments recorded at −2.30 V *vs.* Ag pseudo-reference under N_2 in DCE/MeCN (A) and at −1.85 V *vs.* Ag pseudo-reference under CO_2 in MeCN (B), using 5 mM $^5[Fe^{II}(\mathbf{NP^{iso}})(Cl)](BPh_4)$ and 0.1 M $TBAPF_6$, with Pt grids as working and counter electrodes and an Ag wire as the pseudo-reference electrode.

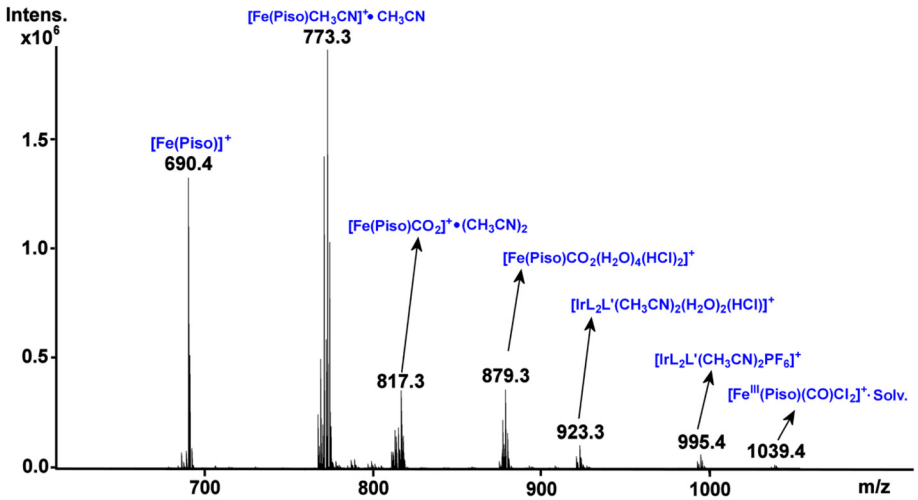

Fig. 5 Positive ESI-MS spectrum of the reaction mixture containing $^{5}[Fe^{II}(\mathbf{NP^{iso}})(Cl)](BPh_4)$ (50 μM), [Ir(dtbbpy)(ppy)$_2$](PF$_6$) (0.2 mM) and BIH (0.1 M) in MeCN/H$_2$O (4.5 : 0.5) after 3 h of reaction time. The isotopic distribution envelopes centered at *m*/*z* 690.40, 773.30, 817.30, 879.30 and 1039.40 correspond to singly charged mononuclear iron species proposed to participate in the catalytic cycle.

$CH_3CN]\cdot CH_3CN\}^+$ $^{4}[Fe^{I}(\mathbf{NP^{iso}})(NCMe)]^+$, respectively (Fig. S27). Additionally, the envelopes centered at *m*/*z* 817.30 and 879.30 are assigned to the subsequent intermediates in the mechanistic cycle, namely $\{[Fe^{I}(P^{iso})CO_2](CH_3CN)_2\}^+$ and $\{[Fe^{I}(P^{iso})CO_2](H_2O)_4(HCl)_2\}^+$, arising from the interaction with CO_2 and coordination of different combinations of solvent molecules. Finally, the envelopes centered at *m*/*z* 923.3 and 995.4 are assigned to the photosensitizer-derived species $\{Ir(C_{40}H_{40}N_4)(CH_3CN)_2(H_2O)_2(HCl)\}^+$ and $\{Ir(C_{40}H_{39}N_4)(CH_3CN)_2)PF_6\}^+$ present in the reaction mixture, while a minor signal attributable to $^{5}[Fe^{II}(\mathbf{NP^{iso}})(Cl)](BPh_4)$ in association with CO is also detected (Table S4).

Computational studies

To probe the CO_2 reduction pathways and clarify the underlying redox processes, density functional and correlated *ab initio* calculations were performed. Detailed electronic structure analyses are provided in the SI. All calculations employed the relativistic DKH2-PBE0-D4 density functional method (see Computational details).

The thermodynamics of chloride–acetonitrile substitution were first evaluated across successive reduction states. To minimise artefacts associated with charged fragments, geometries were optimised either as neutral van der Waals adducts, $^{5}[Fe^{II}(P^{iso})Cl]^+\cdots NCMe$, or as ion-paired species, $^{5}[Fe^{II}(P^{iso})(NCMe)]^{2+}\cdots Cl^-$ with superscripts indicating spin multiplicity. The resulting PBE0-D4 free energies systematically overestimated the substitution energetics (Table 3). To obtain reliable energetics, single-point DLPNO-CCSD(T) energies were combined with PBE0-D4 thermal corrections, yielding a consistent thermodynamic description. While the parent $^{5}[Fe^{II}(P^{iso})Cl]^+$ complex is thermodynamically stable, one-electron reduction establishes an equilibrium between chloride-bound and acetonitrile-bound species $^{5}[Fe^{II}(P^{iso})Cl]^+\cdots NCMe \rightleftarrows {}^{5}[Fe^{II}(P^{iso})(NCMe)]^{2+}\cdots Cl^-$, as $\log K \approx -1.2$. Upon a second electron addition, the acetonitrile-coordinated complex becomes thermodynamically favored (Fig. S28 and S29).

These trends are consistent with the experimentally observed solvent-dependent redox behavior.

Reduction potentials were then calculated independently for $[Fe^{II}(\mathbf{NP^{iso}})(Cl)]^+$ and $[Fe^{II}(\mathbf{NP^{iso}})(NCMe)]^{2+}$ to aid assignment of the experimentally observed electrochemical features. The calculated values (Table S5) show good agreement with experiment.

The overall catalytic mechanism was subsequently examined. Given that $[Ir(ppy)_2(dtb\text{-}bpy)]^+$ can act as a hydrogen-atom acceptor and that BIH functions as a protic electron donor, full thermodynamic cycles for coupled proton/electron transfer were evaluated computationally (Fig. S30 and S33 of the SI). The calculated oxidation potential of the iridium complex is +2.26 V. On this basis, the most thermodynamically favorable pathway is summarized in Fig. 6.[76]

The reactivity of $^{5}[Fe^{II}(\mathbf{NP^{iso}})(Cl)]^+$ towards electron reduction, halide dissociation, and MeCN coordination was evaluated. The most favorable sequence involves a $1e^-$ reduction of $^{5}[Fe^{II}(\mathbf{NP^{iso}})(Cl)]^+$ followed by chloride substitution by CH_3CN (ΔG = +1.7 kcal mol^{-1}, Table 3), yielding the adduct $^{4}[Fe^{I}(\mathbf{NP^{iso}})(NCMe)]^+$ as outlined in Fig. 6.

The reaction subsequently proceeds *via* proton-coupled CO_2 uptake at the iron center to form $^{3}[Fe^{II}(\mathbf{NP^{iso}})(CO_2H)]^+$. For this species, the triplet state is the most stable, with the corresponding singlet lying 15 kcal mol^{-1} higher in free energy. Given the atypical nature of the $-CO_2H$ ligand, the electronic structure of this intermediate was analyzed in detail. The formal electronic structure could, in principle, be described as $[Fe^{I}(\mathbf{NP^{iso}})(CO_2H)^0]^+$, $[Fe^{II}(\mathbf{NP^{iso}})(CO_2H)^-]^+$ or $[Fe^{III}(\mathbf{NP^{iso}})(CO_2H)^{2-}]^+$. Given the $3d^6$ electron configuration (Fig. S34), the answer is $[Fe^{II}(\mathbf{NP^{iso}})(CO_2H)^-]^+$, consistent with a high-spin

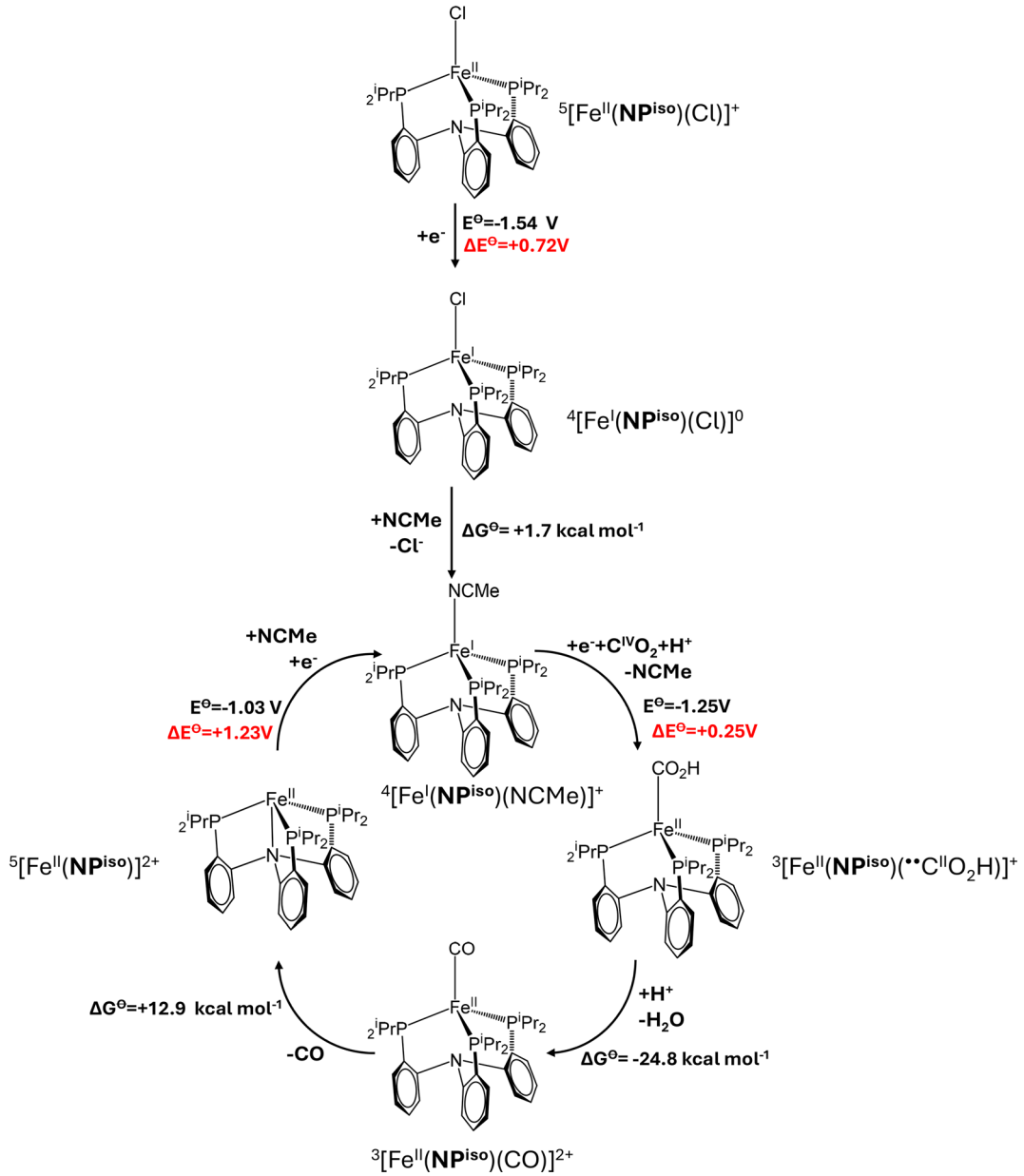

Fig. 6 Summary of the proposed mechanism of the photocatalytic reduction of CO_2 by complex ^{5}[Fe^{II}(NP^{iso})(Cl)]$^+$. In red are the redox potential differences with respect to the single electron reduction by the [Ir(ppy)$_2$(dtb-bpy)]$^+$ complex (with $E^\circ_{ox} = +2.26$ V) or proton coupled reduction.

Table 3 Calculated ligand substitution free energies under successive 1e$^-$ additions

$\Delta G_{298\ K}$/kcal mol^{-1}	PBE0-D4	DLPNO-CCSD(T)
^{5}[Fe^{II}(NP^{iso})(Cl)]$^+$···NCMe → ^{5}[Fe^{II}(NP^{iso})(NCMe)]$^{2+}$···Cl$^-$	+19.3	+13.5
^{4}[Fe^{I}(NP^{iso})(Cl)]^0···NCMe → ^{4}[Fe^{I}(NP^{iso})(NCMe)]$^+$···Cl$^-$	+6.7	+1.7
^{3}[Fe^0(NP^{iso})(Cl)]$^-$···NCMe → ^{3}[Fe^0(NP^{iso})(NCMe)]^0···Cl$^-$	+6.7	−5.3

configuration. Although formation of a CO_2^{2-} adduct was considered, ^{4}[Fe^I(NP^{iso})(NCMe)]$^+$ + CO_2 → ^{4}[Fe^I(NP^{iso})(CO$_2$)]$^+$ + NCMe, direct CO_2 coordination is thermodynamically disfavored (ΔG = +13.0 kcal mol^{-1}). The computational Pourbaix diagram shows that direct access to the doubly reduced species is disfavored (E° = −1.94 V), whereas a proton-coupled electron transfer pathway leading to HCO_2^- formation is thermodynamically preferred (E° = −0.68 V) (Fig. S32 and S33). Accordingly, proton-coupled CO_2 uptake represents the most thermodynamically accessible pathway.

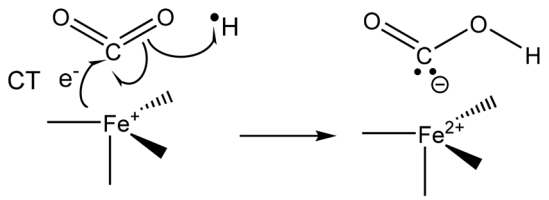

Scheme 1

The metal-assisted ligand reduction/H-atom transfer can be idealized as outlined in Scheme 1:

Subsequent protonation and water elimination yield the carbonyl complex $^{3}[Fe^{II}(\mathbf{NP^{iso}})(CO)]^{2+}$. Because CO is a strong field ligand, the corresponding singlet state was also evaluated. However, this minimum lies 12 kcal mol^{-1} higher in free energy. The degree of metal–ligand backbonding in $^{3}[Fe^{II}(\mathbf{NP^{iso}})(CO_2H)]^{+}$ is markedly lower than in $^{3}[Fe^{II}(\mathbf{NP^{iso}})(CO)]^{2+}$ (see Table S6), emphasizing the predominantly σ-donating character of the CO_2H^- ligand.

CO dissociation from $^{3}[Fe^{II}(\mathbf{NP^{iso}})(CO)]^{2+}$ constitutes the rate-limiting step of the catalytic cycle. Potential-energy scans indicate a barrierless dissociation pathway, with no distinct transition state located. This step is endoenergetic[77] and is not facilitated by further reduction, which instead strengthens metal–carbonyl backbonding and makes CO dissociation more difficult. For example, CO dissociation from $^{2}[Fe^{I}(\mathbf{NP^{iso}})(CO)]^{+}$ and $^{1}[Fe^{0}(\mathbf{NP^{iso}})(CO)]$ reaches electronic energy plateaus of 57 and 75 kcal mol^{-1} respectively (Fig. S35 to S37).

CO dissociation additionally requires consideration of spin-state reorganization. Creation of a coordination vacancy will almost certainly promote a spin crossover, with the quintet state being the most plausible for a 3d^6 complex. A minimum-energy crossing point (MECP) between the triplet and quintet surfaces of $^{3}[Fe^{II}(\mathbf{NP^{iso}})(CO)]^{2+}$ was therefore computed. This MECP lies at a $\Delta G_{298\ K}$ = +10.1 kcal mol^{-1} and is associated with a significantly elongated Fe–C bond. Beyond this point, the quintet minimum $^{5}[Fe^{II}(\mathbf{NP^{iso}})(CO)]^{2+}$ is reached, in which the Fe–C interaction is sufficiently weakened to allow CO dissociation at a free energy of +12.9 kcal mol^{-1} relative to the initial complex (Fig. 7).[78,79]

Regeneration of the catalytically active $^{4}[Fe^{I}(\mathbf{NP^{iso}})(NCMe)]^{+}$ species is strongly favored electrochemically, with this step driven by the photoreduced $[Ir(ppy)_2(dtb\text{-}bpy)(H)]^{+}$ complex and associated with ΔE = +1.23 V. CO dissociation is identified as the sole significantly endergonic and rate-limiting step of the catalytic cycle.

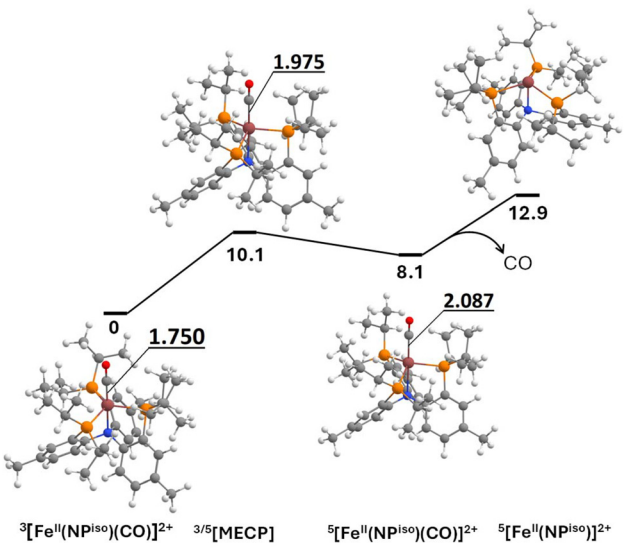

Fig. 7 PBE0-D4 thermal energy profile (free energies in kcal mol^{-1}) for CO dissociation from the complex $^{3}[Fe^{II}(\mathbf{NP^{iso}})(CO)]^{2+}$. Metal-carbonyl bond lengths (Å) are indicated at each point. No transition states were identified.

Conclusions

This study investigates the CO_2-to-CO reduction mechanism under visible-light irradiation of a previously reported pseudo-tetrahedral Fe(II) complex $^{5}[Fe^{II}(\mathbf{NP^{iso}})(Cl)](BPh_4)$, supported by the tripodal $\mathbf{NP^{iso}}$ phosphine backbone. In coordinating MeCN, the system achieves CO turnover numbers exceeding 1300 at micromolar catalyst concentrations and quantum yields of ~0.6% within 3 h, placing its performance among the most active Fe-based photoreduction catalysts to date.

Electrochemical, SEC-IR and emission-quenching data indicate that catalysis is initiated by reductive quenching, generating a 2e$^-$-reduced species, $^{5}[Fe^{II}(\mathbf{NP^{iso}})(Cl)](BPh_4)$, that undergoes Cl^- dissociation and MeCN coordination to form the active Fe(I) complex $^{4}[Fe^{I}(\mathbf{NP^{iso}})(NCMe)]^{+}$. SEC-IR and high-resolution ESI-MS provide evidence for CO_2-bound Fe(I/II)–CO_2H/CO and Fe–CO intermediates. DFT and local-pair coupled-cluster calculations support a Fe(II)–CO_2H^- formulation featuring the ligand-centred reduction/H-atom transfer character, enabling C–O bond activation.

Outer-sphere electron mediators, such as TTA and Fc, significantly enhance the CO selectivity in MeCN, whereas mixed MeCN/H_2O solutions are limited by mediator solubility and competitive deactivation pathways. Altogether, these results establish pseudotetrahedral P_3N/PNP ligand environments as robust, redox-accessible platforms that stabilise reactive Fe intermediates, allow direct observation of CO_2 binding and CO release, and support CO-selective multielectron photoreduction at low catalyst loadings. These mechanistic insights provide a set of design principles for next-generation iron photocatalysts that couple geometric and electronic control to achieve efficient CO_2 conversion.

This work lays the foundation for a new class of geometrically controlled Fe photocatalysts. Future efforts will target ligand architectures that more precisely tune Fe(I/II) redox energetics and mitigate the kinetic barrier associated with CO dissociation. Engineering mediator–catalyst pairings that function effectively in water-rich environments will broaden the applicability toward solar-fuel formulations. Ultimately, extending these design principles to deeper CO_2 reduction

pathways and incorporating ultrafast spectroscopies will enable a molecular-level blueprint for sustainable iron-based CO_2 conversion technologies.

Methods

Computational details

The ORCA[80–83] 6.0.1 program package was used in all the calculations described herein. The PBE0 density functional approximation[84,85] with Grimme's fourth generation dispersion correction[86] was employed (PBE0-D4) along with the second order Douglas–Kroll–Heß relativistic Hamiltonian (DKH2) for all the potential energies and optimizations. The RIJCOSX[86–91] integral approximation technique was employed to expedite calculations. The DKH-def2-TZVP basis set was used for iron and for the remaining elements the DKH-def2-SV(P) basis set was assigned. The auxiliary basis sets for the multi-center integrals were assigned as def2/J[92] to all the elements. The CPCM[93–95] implicit solvent scheme with default parameters for acetonitrile were additionally used in the calculations. Free energies were calculated at 298.15 K and 1 atm pressure. All minima and transition states were characterised by all real and one imaginary vibrational modes respectively. Transition states were traced back to their reagents and products by following a fractional displacement along the imaginary vibrational mode. The Quasi-Harmonic Rigid-Rotor-Harmonic-Oscillator (RRHO) approximation due to Grimme was employed in the computation of enthalpies and entropies.[96]

Additional DLPNO-CCSD(T) calculations[97–101] were run for better potential energy values to gain accurate free energies of NCMe/Cl^- ligand exchange given by $G_{DLPNO} = E_{DLPNO} + (G_{PBE0} - E_{PBE0})$.

The experimental absolute reduction potential value of the ferrocenium/ferrocene pair in acetonitrile was set to 5.22 eV as recommended by Addison and Pavlishchuk.[102] The absolute free energy of a proton in acetonitrile was set to −1056.6 kJ mol^{-1} (−10.95 eV) as recommended by Manassir and Farrokhpour.[103] Reduction potentials of one electron reduced pairs were calculated according to the expression $E = -\Delta G_{PBE0} - 5.22$ V.

Natural bond orbital analyses were performed with the NBO 7.0 program.[104,105]

Author contributions

The manuscript was written through contributions of all authors. All authors have given approval to the final version of the manuscript.

Conflicts of interest

There are no conflicts to declare.

Data availability

The data supporting this article have been included as part of the supplementary information (SI). Supplementary information: experimental details, characterization of the catalyst (additional computational data, ^{1}H NMR spectra, FTIR spectra, UV-vis spectra, cyclic voltammetry, SC-XRD data and tables), spectroscopic monitoring of photocatalytic reactions, and *in situ* generated intermediates by ESI-MS. See DOI: https://doi.org/10.1039/d6dt00909c.

Optimised Cartesian coordinates and electronic energies for all DFT and DLPNO-CCSD(T) calculations are available in the ioChem-BD repository at https://doi.org/10.19061/iochem-bd-6-581. Crystallographic data for the complex were originally reported by MacBeth, Harkins and Peters (*Can. J. Chem.*, 2005, **83**, 332–340) and deposited with the Cambridge Crystallographic Data Centre (CCDC).

Optimized structures are also available for visualization and can be downloaded from the iochem-BD[106,107] database at https://doi.org/10.19061/iochem-bd-6-581.

Acknowledgements

Centro de Química Estrutural (CQE) and Institute of Molecular Sciences (IMS) acknowledge the financial support of Fundação para a Ciência e Tecnologia (Projects UID/00100/2025, UID/PRR/100/2025 and LA/P/0056/2020: https://doi.org/10.54499/LA/P/0056/2020, respectively). This work was also developed within the scope of the project CICECO Aveiro Institute of Materials, UID/50011/2025 (https://doi.org/10.54499/UID/50011/2025) & LA/P/0006/2020 (https://doi.org/10.54499/LA/P/0006/2020), financed by National Funds through the FCT/MCTES (PIDDAC). P. N. M. thanks FCT for financial support, grant PTDC/QUI-QIN/0252/2021: https://doi.org/10.54499/PTDC/QUI-QIN/0252/2021, for the co-financing by the PRR – Recovery and Resilience Plan of the European Union and for the contract 2023.15441.TENURE.003/CP00003/CT00011. S. R. thanks FCT for the contract 2020.02134.CEECIND: https://doi.org/10.54499/2020.02134.CEECIND/CP1605/CT0002. M. A. B. thanks FCT for the PhD scholarship (2021.07918.BD: https://doi.org/10.54499/2021.07918.BD). N. A. G. B. gratefully acknowledges Fundação para a Ciência e a Tecnologia for the FCT/DL57 researcher (https://doi.org/10.54499/DL57/2016/CP1479/CT0050) fund, BioISI unit funding (UIDB/04046/2025, https://doi.org/10.54499/UIDB/04046/2020 and https://doi.org/10.54499/UIDP/04046/2020), high-performance computing grant 2025.00002. HPCVLAB.ISTUL, and Prof. Frank Neese for providing access to computational infrastructure. COST Actions CA21101 (COSY), CA21127 (TrANsMIT) and CA22131 (LUCES) are also acknowledged. H. N. M. thanks the University of Glasgow for supporting this work and Prof. Lee Cronin for providing access to the ESI-MS facilities. Open Access funding provided by the Max Planck Society.

References

1 J. Artz, T. E. Müller, K. Thenert, J. Kleinekorte, R. Meys, A. Sternberg, A. Bardow and W. Leitner, Sustainable Conversion of Carbon Dioxide: An Integrated Review of Catalysis and Life Cycle Assessment, *Chem. Rev.*, 2018, **118**, 434–504, DOI: 10.1021/acs.chemrev.7b00435.

2 C. D. Windle and R. N. Perutz, Advances in Molecular Photocatalytic and Electrocatalytic CO_2 Reduction, *Coord. Chem. Rev.*, 2012, **256**, 2562–2570, DOI: 10.1016/j.ccr.2012.03.010.

3 J. Bonin, A. Maurin and M. Robert, Molecular Catalysis of the Electrochemical and Photochemical Reduction of CO_2 with Fe and Co metal based complexes: recent advances, *Coord. Chem. Rev.*, 2017, **334**, 184–198, DOI: 10.1016/j.ccr.2016.09.005.

4 H. Takeda, C. Cometto, O. Ishitani and M. Robert, Electrons, photons, protons and earth-abundant metal complexes for molecular catalysis of CO_2 reduction, *ACS Catal.*, 2017, **7**, 70–88, DOI: 10.1021/acscatal.6b02181.

5 Y. Yamazaki, H. Takeda and O. Ishitani, Photocatalytic reduction of CO_2 using metal complexes, *J. Photochem. Photobiol., C*, 2015, **25**, 106–137, DOI: 10.1016/j.jphotochemrev.2015.09.001.

6 H. Takeda, K. Ohashi, A. Sekine and O. Ishitani, Photocatalytic CO_2 reduction using Cu(I) photosensitizers with a Fe(II) catalyst, *J. Am. Chem. Soc.*, 2016, **138**, 4354–4357, DOI: 10.1021/jacs.6b01970.

7 E. Bassan, R. Inoue, D. Fabry, F. Calogero, S. Potenti, A. Gualandi, P. G. Cozzi, K. Kamogawa, P. Ceroni, Y. Tamaki and O. Ishitani, Visible-light driven photocatalytic CO_2 reduction promoted by organic photosensitizers and a Mn(I) catalyst, *Sustainable Energy Fuels*, 2023, **7**, 3454–3463, DOI: 10.1039/d3se00546a.

8 K. K. Chen, S. Guo, M. J. Ding, T. B. Lu and Z. M. Zhang, Heavy-atom-free photosensitizers for high-yield CO_2-to-CO conversion, *CCS Chem.*, 2023, **5**, 2650–2662, DOI: 10.31635/ccschem.023.202202365.

9 A. Call, M. Cibian, K. Yamamoto, T. Nakazono, K. Yamauchi and K. Sakai, Highly efficient and selective photocatalytic CO_2 reduction to CO in water by a cobalt porphyrin molecular catalyst, *ACS Catal.*, 2019, **9**, 4867–4874, DOI: 10.1021/acscatal.8b04975.

10 Y. Wei, L. Chen, H. Chen, L. Cai, G. Tan, Y. Qiu, Q. Xiang, G. Chen, T. C. Lau and M. Robert, Highly efficient photocatalytic reduction of CO_2 to CO by in situ formation of a hybrid catalytic system based on molecular iron quaterpyridine covalently linked to carbon nitride, *Angew. Chem., Int. Ed.*, 2022, **61**, e202116832, DOI: 10.1002/anie.202116832.

11 F. A. Rahimi, S. Dey, P. Verma and T. K. Maji, Photocatalytic CO_2 reduction based on a Re(I)-integrated conjugated microporous polymer: role of a sacrificial electron donor in product selectivity and efficiency, *ACS Catal.*, 2023, **13**, 5969–5978, DOI: 10.1021/acscatal.3c00053.

12 R. N. Sampaio, D. C. Grills, D. E. Polyansky, D. J. Szalda and E. Fujita, Unexpected roles of triethanolamine in the photochemical reduction of CO_2 to formate by ruthenium complexes, *J. Am. Chem. Soc.*, 2020, **142**, 2413–2428, DOI: 10.1021/jacs.9b11897.

13 H. Takeda, Y. Monma and O. Ishitani, Highly functional dinuclear CuI-complex photosensitizers for photocatalytic CO_2 reduction, *ACS Catal.*, 2021, **11**, 11973–11984, DOI: 10.1021/acscatal.1c03336.

14 H. Takeda, M. Irimajiri, T. Mizutani, S. Nozawa, Y. Matsuura, M. Kurosu and O. Ishitani, Photocatalytic CO_2 reduction using mixed catalytic systems comprising an iron cation with bulky phenanthroline ligands, *Inorg. Chem.*, 2024, **63**, 7343–7355, DOI: 10.1021/acs.inorgchem.4c00247.

15 E. Boutin, L. Merakeb, B. Ma, B. Boudy, M. Wang, J. Bonin, E. Anxolabéhère-Mallart and M. Robert, Molecular catalysis of CO_2 reduction: recent advances and perspectives in electrochemical and light-driven processes with selected Fe, Ni and Co aza macrocyclic and polypyridine complexes, *Chem. Soc. Rev.*, 2020, **49**, 5772–5809, DOI: 10.1039/d0cs00218f.

16 D. C. Liu, D. C. Zhong and T. B. Lu, Non-noble metal-based molecular complexes for CO_2 reduction: from the ligand design perspective, *Energy Chem.*, 2020, **2**, 100034, DOI: 10.1016/j.enchem.2020.100034.

17 T. Dhanasekaran, J. Grodkowski, P. Neta, P. Hambright and E. Fujita, p-Terphenyl-sensitized photoreduction of CO_2 with cobalt and iron porphyrins: interaction between CO and reduced metalloporphyrins, *J. Phys. Chem. A*, 1999, **103**, 7742–7748, DOI: 10.1021/jp991423u.

18 S. Amanullah, P. Saha and A. Dey, Activating the Fe(I) state of iron porphyrinoid with second-sphere proton transfer residues for selective reduction of CO_2 to HCOOH via Fe(III/II)-COOH intermediate(s), *J. Am. Chem. Soc.*, 2021, **143**, 13579–13592, DOI: 10.1021/jacs.1c04392.

19 Y. Okabe, S. K. Lee, M. Kondo and S. Masaoka, Syntheses and CO_2 reduction activities of π-expanded/extended iron porphyrin complexes, *J. Biol. Inorg. Chem.*, 2017, **22**, 713–725, DOI: 10.1007/s00775-017-1438-3.

20 B. Mondal, A. Rana, P. Sen and A. Dey, Intermediates involved in the $2e^-/2H^+$ reduction of CO_2 to CO by iron(0) porphyrin, *J. Am. Chem. Soc.*, 2015, **137**, 11214–11217, DOI: 10.1021/jacs.5b05992.

21 K. Guo, X. Li, H. Lei, H. Guo, X. Jin, X. P. Zhang, W. Zhang, U. P. Apfel and R. Cao, Role-specialized division of labor in CO_2 reduction with doubly-functionalized iron porphyrin atropisomers, *Angew. Chem., Int. Ed.*, 2022, **61**, e202209602, DOI: 10.1002/anie.202209602.

22 M. Imai, K. Kosugi, Y. Saga, M. Kondo and S. Masaoka, Introducing proton/electron mediators enhances the catalytic ability of an iron porphyrin complex for photochemical CO_2 reduction, *Chem. Commun.*, 2023, **59**, 10741–10744, DOI: 10.1039/d3cc01862h.

23 P. Sen, B. Mondal, D. Saha, A. Rana and A. Dey, Role of 2^{nd} sphere H-bonding residues in tuning the kinetics of

CO_2 reduction to CO by iron porphyrin complexes, *Dalton Trans.*, 2019, **48**, 5965–5977, DOI: 10.1039/c8dt03850c.

24 Y. K. Zhang, L. Zhao, W. J. Xie, H. R. Li and L. N. He, Mononuclear iron pyridinethiolate complex promoted CO_2 photoreduction via rapid intramolecular electron transfer, *ChemSusChem*, 2024, **17**, e202400090, DOI: 10.1002/cssc.202400090.

25 H. R. Lewine, A. G. Teigen, A. M. Trausch, K. M. Lindblom, T. Seda, E. W. Reinheimer, T. Kowalczyk and J. D. Gilbertson, Sequential deoxygenation of CO_2 and NO_2^- via redox-control of a pyridinediimine ligand with a hemilabile phosphine, *Inorg. Chem.*, 2023, **62**, 15173–15179, DOI: 10.1021/acs.inorgchem.3c02323.

26 Z. Guo, S. Cheng, C. Cometto, E. Anxolabéhère-Mallart, S. M. Ng, C. C. Ko, G. Liu, L. Chen, M. Robert and T. C. Lau, Highly efficient and selective photocatalytic CO_2 reduction by iron and cobalt quaterpyridine complexes, *J. Am. Chem. Soc.*, 2016, **138**, 9413–9416, DOI: 10.1021/jacs.6b06002.

27 N. Elgrishi, M. B. Chambers, X. Wang and M. Fontecave, Molecular polypyridine-based metal complexes as catalysts for the reduction of CO_2, *Chem. Soc. Rev.*, 2017, **46**, 761–796, DOI: 10.1039/c5cs00391a.

28 F. Droghetti, F. Lemken, L. Rulíšek, A. Ruggi and M. Natali, Selective and efficient light-driven CO_2 reduction to CO with a heptacoordinated polypyridine iron(II) catalyst, *ACS Catal.*, 2024, **14**, 16920–16935, DOI: 10.1021/acscatal.4c04290.

29 F. Droghetti, L. Villa, A. Sartorel, L. Dell'Amico, A. Ruggi and M. Natali, Boosting light-driven CO_2 conversion into CO by a polypyridine iron(II) catalyst using an organic sensitizer, *ChemSusChem*, 2025, **18**, e202402627, DOI: 10.1002/cssc.202402627.

30 X. Z. Wang, S. L. Meng, J. Y. Chen, H. X. Wang, Y. Wang, S. Zhou, X. B. Li, R. Z. Liao, C. H. Tung and L. Z. Wu, Mechanistic insights into iron(II) bis(pyridyl)amine-bipyridine skeleton for selective CO_2 photoreduction, *Angew. Chem., Int. Ed.*, 2021, **60**, 26072–26079, DOI: 10.1002/anie.202107386.

31 P. De La Torre, J. S. Derrick, A. Snider, P. T. Smith, M. Loipersberger, M. Head-Gordon and C. J. Chang, Exchange coupling determines metal-dependent efficiency for iron- and cobalt-catalyzed photochemical CO_2 reduction, *ACS Catal.*, 2022, **12**, 8484–8493, DOI: 10.1021/acscatal.2c02072.

32 P. G. Alsabeh, A. Rosas-Hernández, E. Barsch, H. Junge, R. Ludwig and M. Beller, Iron-catalyzed photoreduction of carbon dioxide to synthesis gas, *Catal. Sci. Technol.*, 2016, **6**, 3623–3630, DOI: 10.1039/c5cy01129a.

33 T. Wakabayashi, K. Kamada, K. Sekizawa, S. Sato, T. Morikawa, J. Jung and S. Saito, Photocatalytic CO_2 reduction using an iron-bipyridyl complex supported by two phosphines for improving catalyst durability, *Organometallics*, 2022, **41**, 1865–1871, DOI: 10.1021/acs.organomet.2c00171.

34 J. Bonin, M. Robert and M. Routier, Selective and efficient photocatalytic CO_2 reduction to CO using visible light and an iron-based homogeneous catalyst, *J. Am. Chem. Soc.*, 2014, **136**, 16768–16771, DOI: 10.1021/ja510290t.

35 N. El Aouni, A. Aghmiz, M. Reguero and A. M. Masdeu-Bultó, Iron, cobalt and nickel complexes with N4-donor ligands catalysts for the CO_2 photoreduction, *Mol. Catal.*, 2024, **565**, 114392, DOI: 10.1016/j.mcat.2024.114392.

36 T. Liu, L. Chen and D. Chao, Noble metal-free bis-tridentate benzimidazole zinc(II) and iron(II) complexes for selective CO_2 photoreduction, *Dalton Trans.*, 2022, **51**, 4052–4057, DOI: 10.1039/d2dt00226d.

37 A. Rosas-Hernández, C. Steinlechner, H. Junge and M. Beller, Earth-abundant photocatalytic systems for the visible-light-driven reduction of CO_2 to CO, *Green Chem.*, 2017, **19**, 2356–2360, DOI: 10.1039/c6gc03527b.

38 E. Oberem, A. F. Roesel, A. Rosas-Hernández, T. Kull, S. Fischer, A. Spannenberg, H. Junge, M. Beller, R. Ludwig, M. Roemelt and R. Francke, Mechanistic insights into the electrochemical reduction of CO_2 catalyzed by iron cyclopentadienone complexes, *Organometallics*, 2019, **38**, 1236–1247, DOI: 10.1021/acs.organomet.8b00517.

39 Y. Qin, L. Chen, G. Chen, Z. Guo, L. Wang, H. Fan, M. Robert and T. C. Lau, A highly active and robust iron quinquepyridine complex for photocatalytic CO_2 reduction in aqueous acetonitrile solution, *Chem. Commun.*, 2020, **56**, 6249–6252, DOI: 10.1039/d0cc01930e.

40 Y. Xiao, H. T. Zhang and M. T. Zhang, Heterobimetallic NiFe complex for photocatalytic CO_2 reduction: united efforts of NiFe dual sites, *J. Am. Chem. Soc.*, 2024, **146**, 28832–28844, DOI: 10.1021/jacs.4c08510.

41 I. Cocosila, A. Solé-Daura, P. Gotico, J. Forte, Y. Li and M. Fontecave, Visible-light-driven carbon dioxide reduction catalyzed by iron Schiff-base complexes, *ACS Catal.*, 2024, **14**, 9618–9627, DOI: 10.1021/acscatal.4c01639.

42 H. Fong and J. C. Peters, Hydricity of an Fe–H species and catalytic CO_2 hydrogenation, *Inorg. Chem.*, 2015, **54**, 5124–5135, DOI: 10.1021/ic502508p.

43 Y. Lee and J. C. Peters, Silylation of iron-bound carbon monoxide affords a terminal Fe carbyne, *J. Am. Chem. Soc.*, 2011, **133**, 4438–4446, DOI: 10.1021/ja109678y.

44 J. Rittle and J. C. Peters, Fe–N_2/CO complexes that model a possible role for the interstitial C atom of FeMo-cofactor (FeMoco), *Proc. Natl. Acad. Sci. U. S. A.*, 2013, **110**, 15898–15903, DOI: 10.1073/pnas.1310153110.

45 T. A. Betley and J. C. Peters, A tetrahedrally coordinated L_3Fe–N_x platform that accommodates terminal nitride (FeIV≡N) and dinitrogen (FeI–N_2–FeI) ligands, *J. Am. Chem. Soc.*, 2004, **126**, 6252–6254, DOI: 10.1021/ja048713v.

46 T. A. Betley and J. C. Peters, Dinitrogen chemistry from trigonally coordinated iron and cobalt platforms, *J. Am. Chem. Soc.*, 2003, **125**, 10782–10783, DOI: 10.1021/ja036687f.

47 C. T. Saouma, M. W. Day and J. C. Peters, CO_2 reduction by Fe(I): solvent control of C–O cleavage versus C–C coup-

ling, *Chem. Sci.*, 2013, **4**, 4042–4051, DOI: 10.1039/c3sc51262b.

48 C. E. MacBeth, S. B. Harkins and J. C. Peters, Synthesis and characterization of cationic iron complexes supported by neutral ligands NP^{i-Pr}_3, $NArP^{i-Pr}_3$ and NS^{t-Bu}_3, *Can. J. Chem.*, 2005, **83**, 332–340, DOI: 10.1139/v05-017.

49 C. C. Lu, C. T. Saouma, M. W. Day and J. C. Peters, Fe(I)-mediated reductive cleavage and coupling of CO_2: an FeII (μ-O,μ-CO)FeII core, *J. Am. Chem. Soc.*, 2007, **129**, 4–5, DOI: 10.1021/ja065524z.

50 C. Ziebart, C. Federsel, P. Anbarasan, R. Jackstell, W. Baumann, A. Spannenberg and M. Beller, Well-defined iron catalyst for improved hydrogenation of carbon dioxide and bicarbonate, *J. Am. Chem. Soc.*, 2012, **134**, 20701–20704, DOI: 10.1021/ja307924a.

51 C. Federsel, A. Boddien, R. Jackstell, R. Jennerjahn, P. J. Dyson, R. Scopelliti, G. Laurenczy and M. Beller, A well-defined iron catalyst for the reduction of bicarbonates and carbon dioxide to formates, alkyl formates and formamides, *Angew. Chem., Int. Ed.*, 2010, **49**, 9777–9780, DOI: 10.1002/anie.201004263.

52 B. Mondal, F. Neese and S. Ye, Control in the rate-determining step provides a promising strategy to develop new catalysts for CO_2 hydrogenation: a local pair natural orbital coupled cluster theory study, *Inorg. Chem.*, 2015, **54**, 7192–7198, DOI: 10.1021/acs.inorgchem.5b00469.

53 B. Mondal, F. Neese and S. Ye, Toward rational design of 3d transition metal catalysts for CO_2 hydrogenation based on insights into hydricity-controlled rate-determining steps, *Inorg. Chem.*, 2016, **55**, 5438–5444, DOI: 10.1021/acs.inorgchem.6b00471.

54 J. S. Anderson, J. Rittle and J. C. Peters, Catalytic conversion of nitrogen to ammonia by an iron model complex, *Nature*, 2013, **501**, 84–87, DOI: 10.1038/nature12435.

55 Y. Lee, N. P. Mankad and J. C. Peters, Triggering N_2 uptake via redox-induced expulsion of coordinated NH_3 and N_2 silylation at trigonal bipyramidal iron, *Nat. Chem.*, 2010, **2**, 558–565, DOI: 10.1038/nchem.660.

56 J. S. Anderson, M. E. Moret and J. C. Peters, Conversion of Fe–NH_2 to Fe–N_2 with release of NH_3, *J. Am. Chem. Soc.*, 2013, **135**, 534–537, DOI: 10.1021/ja307714m.

57 J. Chen, D. J. Szalda, E. Fujita and C. Creutz, Iron(II) and ruthenium(II) complexes containing P, N and H ligands: structure, spectroscopy, electrochemistry and reactivity, *Inorg. Chem.*, 2010, **49**, 9380–9391, DOI: 10.1021/ic101077t.

58 T. Shimoda, T. Morishima, K. Kodama, T. Hirose, D. E. Polyansky, G. F. Manbeck, J. T. Muckerman and E. Fujita, Photocatalytic CO_2 reduction by trigonal-bipyramidal cobalt(II) polypyridyl complexes: the nature of cobalt(I) and cobalt(0) complexes upon their reactions with CO_2, CO, or proton, *Inorg. Chem.*, 2018, **57**, 5486–5498, DOI: 10.1021/acs.inorgchem.8b00433.

59 B. Shan and R. Schmehl, Photochemical generation of strong one-electron reductants via light-induced electron transfer with reversible donors followed by cross reaction with sacrificial donors, *J. Phys. Chem. A*, 2014, **118**, 10400–10406, DOI: 10.1021/jp503901v.

60 F. Dumur, Recent advances on ferrocene-based photoinitiating systems, *Eur. Polym. J.*, 2021, **147**, 110328, DOI: 10.1016/j.eurpolymj.2021.110328.

61 K. Mase, K. Ohkubo and S. Fukuzumi, Efficient two-electron reduction of dioxygen to hydrogen peroxide with one-electron reductants with a small overpotential catalyzed by a cobalt chlorin complex, *J. Am. Chem. Soc.*, 2013, **135**, 2800–2808, DOI: 10.1021/ja312199h.

62 T. Wang and D. Astruc, Electron-reservoir applications of ferrocenes and other late transition-metal sandwich complexes: flow batteries, sensing, catalysis and biomedicine, *Coord. Chem. Rev.*, 2025, **524**, 216300, DOI: 10.1016/j.ccr.2024.216300.

63 Y. Tanabe, K. Nakajima and Y. Nishibayashi, Phosphine oxidation with water and ferrocenium(III) cation induced by visible-light irradiation, *Chem. – Eur. J.*, 2018, **24**, 18618–18622, DOI: 10.1002/chem.201805129.

64 B. H. Wilson, H. S. Scott, R. J. Archer, C. Mathonière, R. Clérac and P. E. Kruger, Solution-state spin crossover in a family of $[Fe(L)_2(CH_3CN)_2](BF_4)_2$ complexes, *Magnetochemistry*, 2019, **5**, 22, DOI: 10.3390/magnetochemistry5020022.

65 J. Shon, D. Kim, M. D. Rathnayake, S. Sittel, J. Weaver and T. S. Teets, Photoredox catalysis on unactivated substrates with strongly reducing iridium photosensitizers, *Chem. Sci.*, 2021, **12**, 4069–4078, DOI: 10.1039/d0sc06306a.

66 O. Yurchenko, S. Greiner, A. Hasse, T. Schubert, M. Jänsch and F. Würthner, Electrochemically induced reversible and irreversible coupling of triarylamines, *J. Phys. Chem. B*, 2012, **116**, 30–39, DOI: 10.1021/jp208076z.

67 R. M. Henry, R. K. Shoemaker, R. H. Newell, G. M. Jacobsen, D. L. DuBois and M. R. DuBois, Stereochemical control of iron(II) complexes containing a diphosphine ligand with a pendant nitrogen base, *Organometallics*, 2005, **24**, 2481–2491, DOI: 10.1021/om050071c.

68 H. M. Hüppe, L. Iffland-Mühlhaus, J. Heck, M. Eilers, H. Gildenast, S. Schönfeld, A. Dürrmann, A. Hoffmann, B. Weber, U. P. Apfel and S. Herres-Pawlis, Triflate vs acetonitrile: understanding the iron(II)-based coordination chemistry of tri(quinolin-8-yl)amine, *Inorg. Chem.*, 2023, **62**, 4435–4455, DOI: 10.1021/acs.inorgchem.2c03890.

69 L.-L. Gracia, E. Barani, J. Braun, A. B. Carter, O. Fuhr, A. K. Powell, K. Fink and C. Bizzarri, Photocatalytic reduction of CO_2 by highly efficient homogeneous FeII catalyst based on 2,6-bis(1′,2′,3′-triazolyl-methyl)pyridine: comparison with analogues, *ChemCatChem*, 2022, **14**, e202201163, DOI: 10.1002/cctc.202201163.

70 J. Chen and W. R. Browne, Photochemistry of iron complexes, *Coord. Chem. Rev.*, 2018, **374**, 15–35, DOI: 10.1016/j.ccr.2018.06.008.

71 C. S. Jackson, S. Schmitt, Q. P. Dou and J. J. Kodanko, Synthesis, characterization and reactivity of the stable iron carbonyl complex $[Fe(CO)(N_4Py)](ClO_4)_2$: photoactivated

carbon monoxide release, growth inhibitory activity and peptide ligation, *Inorg. Chem.*, 2011, **50**, 5336–5338, DOI: 10.1021/ic200676s.

72 H. N. Miras, E. F. Wilson and L. Cronin, Unravelling the complexities of inorganic and supramolecular self-assembly in solution with electrospray and cryospray mass spectrometry, *Chem. Commun.*, 2009, 1297–1311, DOI: 10.1039/b819534j.

73 H. N. Miras, M. Sorus, J. Hawkett, D. O. Sells, E. L. McInnes and L. Cronin, Oscillatory template exchange in polyoxometalate capsules: a ligand-triggered, redox-powered, chemically damped oscillation, *J. Am. Chem. Soc.*, 2012, **134**, 6980–6983, DOI: 10.1021/ja302861z.

74 H. N. Miras, D. Stone, D. L. Long, E. L. McInnes, P. Kögerler and L. Cronin, Exploring the structure and properties of transition metal templated $\{VM_{17}(VO_4)_2\}$ Dawson-like capsules, *Inorg. Chem.*, 2011, **50**, 8384–8839, DOI: 10.1021/ic200943s.

75 H. N. Miras, D. L. Long, P. Kögerler and L. Cronin, Bridging the gap between solution and solid-state studies in polyoxometalate chemistry: discovery of a family of $[V_1M_{17}]$-based cages encapsulating two {(VO$_4$)-O-V} moieties, *Dalton Trans.*, 2008, 214–221, DOI: 10.1039/b714285d.

76 T. U. Connell, C. L. Fraser, M. L. Czyz, Z. M. Smith, D. J. Hayne, E. H. Doeven, J. Agugiaro, D. J. D. Wilson, J. L. Adcock, A. D. Scully, D. E. Gómez, N. W. Barnett, A. Polyzos and P. S. Francis, The tandem photoredox catalysis mechanism of $[Ir(ppy)_2(dtb\text{-}bpy)]^+$ enabling access to energy demanding organic substrates, *J. Am. Chem. Soc.*, 2019, **141**, 17646–17658, DOI: 10.1021/jacs.9b07370.

77 M. Loipersberger, D. G. A. Cabral, D. B. K. Chu and M. Head-Gordon, Mechanistic insights into Co and Fe quaterpyridine-based CO_2 reduction catalysts: metal–ligand orbital interaction as the key driving force for distinct pathways, *J. Am. Chem. Soc.*, 2021, **143**, 744–763, DOI: 10.1021/jacs.0c09380.

78 J. N. Harvey, DFT Computation of Relative Spin-State Energetics of Transition Metal Compounds, in *Principles and Applications of Density Functional Theory in Inorganic Chemistry I. Structure and Bonding*, Springer, Berlin, Heidelberg, 2004, vol. 112. DOI: 10.1007/b97939.

79 J. N. Harvey, Spin-forbidden reactions: computational insight into mechanisms and kinetics, *Wiley Interdiscip. Rev.: Comput. Mol. Sci.*, 2014, **4**, 1–14, DOI: 10.1002/wcms.1154.

80 F. Neese, The ORCA program system, *Wiley Interdiscip. Rev.: Comput. Mol. Sci.*, 2012, **2**, 73–78, DOI: 10.1002/wcms.81.

81 F. Neese, Software update: the ORCA program system, version 4.0, *Wiley Interdiscip. Rev.: Comput. Mol. Sci.*, 2018, **8**, e1327, DOI: 10.1002/wcms.1327.

82 F. Neese, F. Wennmohs, U. Becker and C. Riplinger, The ORCA quantum chemistry program package, *J. Chem. Phys.*, 2020, **152**, 224108, DOI: 10.1063/5.0004608.

83 F. Neese, Software update: the ORCA program system-version 6.0, *Wiley Interdiscip. Rev.: Comput. Mol. Sci.*, 2025, **15**, e70019, DOI: 10.1002/wcms.70019.

84 C. Adamo and V. Barone, Exchange functionals with improved long-range behavior and adiabatic connection methods without adjustable parameters: the mPW and mPW1PW models, *J. Chem. Phys.*, 1998, **108**, 664–675, DOI: 10.1063/1.475428.

85 C. Adamo and V. Barone, Toward chemical accuracy in the computation of NMR shieldings: the PBE0 model, *Chem. Phys. Lett.*, 1998, **298**, 113–119, DOI: 10.1016/S0009-2614(98)01201-9.

86 E. Caldeweyher, C. Bannwarth and S. Grimme, Extension of the D3 dispersion coefficient model, *J. Chem. Phys.*, 2017, **147**, 034112, DOI: 10.1063/1.4993215.

87 F. Neese, An improvement of the resolution of the identity approximation for the formation of the Coulomb matrix, *J. Comput. Chem.*, 2003, **24**, 1740–1747, DOI: 10.1002/jcc.10318.

88 F. Neese, F. Wennmohs, A. Hansen and U. Becker, Efficient, approximate and parallel Hartree–Fock and hybrid DFT calculations: a 'chain-of-spheres' algorithm for the Hartree–Fock exchange, *Chem. Phys.*, 2009, **356**, 98–109, DOI: 10.1016/j.chemphys.2008.10.036.

89 S. Kossmann and F. Neese, Comparison of two efficient approximate Hartree–Fock approaches, *Chem. Phys. Lett.*, 2009, **481**, 240–243, DOI: 10.1016/j.cplett.2009.09.073.

90 B. Helmich-Paris, B. Souza, F. Neese and R. Izsák, An improved chain of spheres for exchange algorithm, *J. Chem. Phys.*, 2021, **155**, 104109, DOI: 10.1063/5.0058766.

91 F. Neese, The SHARK integral generation and digestion system, *J. Comput. Chem.*, 2023, **44**, 381–396, DOI: 10.1002/jcc.26942.

92 F. Weigend, Accurate Coulomb-fitting basis sets for H to Rn, Phys, *Chem. Chem. Phys.*, 2006, **8**, 1057–1065, DOI: 10.1039/b515623h.

93 V. Barone and M. Cossi, Quantum calculation of molecular energies and energy gradients in solution by a conductor solvent model, *J. Phys. Chem. A*, 1998, **102**, 1995–2001, DOI: 10.1021/jp9716997.

94 M. Garcia-Ratés and F. Neese, Efficient implementation of the analytical second derivatives of Hartree–Fock and hybrid DFT energies within the framework of the conductor-like polarizable continuum model, *J. Comput. Chem.*, 2019, **40**, 1816–1828, DOI: 10.1002/jcc.25833.

95 M. Garcia-Ratés and F. Neese, Effect of the solute cavity on the solvation energy and its derivatives within the framework of the Gaussian charge scheme, *J. Comput. Chem.*, 2020, **41**, 922–939, DOI: 10.1002/jcc.26139.

96 S. Grimme, Supramolecular binding thermodynamics by dispersion-corrected density functional theory, *Chem. – Eur. J.*, 2012, **18**, 9955–9964, DOI: 10.1002/chem.201200497.

97 F. Neese, A. Hansen and D. G. Liakos, Efficient and accurate approximations to the local coupled cluster singles doubles method using a truncated pair natural orbital

basis, *J. Chem. Phys.*, 2009, **131**, 064103, DOI: 10.1063/1.3173827.

98 F. Neese, F. Wennmohs and A. Hansen, Efficient and accurate local approximations to coupled-electron pair approaches: an attempt to revive the pair natural orbital method, *J. Chem. Phys.*, 2009, **130**, 114108, DOI: 10.1063/1.3086717.

99 A. Hansen, D. G. Liakos and F. Neese, Efficient and accurate local single reference correlation methods for high-spin open-shell molecules using pair natural orbitals, *J. Chem. Phys.*, 2011, **135**, 214102, DOI: 10.1063/1.3663855.

100 C. Riplinger and F. Neese, An efficient and near linear scaling pair natural orbital based local coupled cluster method, *J. Chem. Phys.*, 2013, **138**, 034106, DOI: 10.1063/1.4773581.

101 C. Riplinger, P. Pinski, U. Becker, E. F. Valeev and F. Neese, Sparse maps—a systematic infrastructure for reduced-scaling electronic structure methods: II. linear scaling domain based pair natural orbital coupled cluster theory, *J. Chem. Phys.*, 2016, **144**, 024109, DOI: 10.1063/1.4939030.

102 V. V. Pavlishchuk and A. W. Addison, Conversion constants for redox potentials measured versus different reference electrodes in acetonitrile solutions at 25 °C, *Inorg. Chim. Acta*, 2000, **298**, 97–102, DOI: 10.1016/S0020-1693(99)00407-7.

103 H. Farrokhpour and M. Manassir, Approach for predicting the standard free energy solvation of H+ and acidity constant in nonaqueous organic solvents, *J. Chem. Eng. Data*, 2014, **59**, 3555–3564, DOI: 10.1021/je500459x.

104 E. D. Glendening, C. R. Landis and F. Weinhold, NBO 7.0: new vistas in localized and delocalized chemical bonding theory, *J. Comput. Chem.*, 2019, **40**, 2234–2241, DOI: 10.1002/jcc.25873.

105 E. D. Glendening, C. R. Landis and F. Weinhold, Natural bond orbital methods, *Wiley Interdiscip. Rev.: Comput. Mol. Sci.*, 2012, **2**, 1–42, DOI: 10.1002/wcms.51.

106 M. Álvarez-Moreno, C. de Graaf, N. López, F. Maseras, J. M. Poblet and C. Bo, Managing the computational chemistry big data problem: the ioChem-BD platform, *J. Chem. Inf. Model.*, 2015, **55**, 95–103, DOI: 10.1021/ci500593j.

107 C. Bo, F. Maseras and N. López, The role of computational results databases in accelerating the discovery of catalysts, *Nat. Catal.*, 2018, **1**, 809–810, DOI: 10.1038/s41929-018-0176-4.